JOURNAL OF MATERIALS SCIENCE 30 (1995) 2859–2865

Strength, hardness and fracture toughness of a complex nickel silicide containing ductile phase particles

Z. LI, E. M. SCHULSON
Thayer School of Engineering, Dartmouth College, Hanover, NH 03755, USA

Measurements have been made at room temperature of the strength and fracture toughness of a complex nickel silicide containing particles of a ductile phase. The matrix was either a single-phase $L1_2$ distorted Ni_3Si (β_2) or a two-phase Ni_3Si (β_1) and $Ni_{31}Si_{12}$ (γ) mixture. The particles were a solid solution of Ni(Si) encased within a rim of β_1; they contained a dispersion of β_1 precipitates. The principal variable was the particle size, and this had little effect on the properties. The results show that the compressive yield strength ($\simeq$ 1200 MPa), the compressive ductility (2–10%) and the fracture toughness (17 ± 3 MPa $m^{1/2}$) are relatively high. The toughness and ductility are attributed to the plastic deformation and ductile fracture of the crack-stopping Ni(Si) particles.

1. Introduction

Several recent studies [1–5] have shown that the incorporation of a ductile phase within an intermetallic matrix can improve the mechanical properties of an otherwise brittle material. For instance, niobium provides significant toughening of the intermetallic Nb_5Si_3 in the extruded condition [4, 5]. Similarly, a TiNb phase significantly raises the fracture toughness of TiAl [2]. The primary mechanism which accounts for the improvements is crack bridging by the ductile phase. The bridges deform plastically while cracks grow and thereby contribute a significant amount of plastic work to the toughness of the material.

The present study was performed with ductile phase toughening in mind. The objective was to demonstrate that moderate toughness could be imparted to a complex nickel silicide by incorporating particles of a Ni(Si) solid solution within the microstructure. The particles, as will be shown, contained coherent precipitates of Ni_3Si, and were encased within a shell of Ni_3Si, features which, although not investigated here, may also help to impart good properties at elevated temperatures owing to the anomalous thermal strengthening of Ni_3Si [6]. In addition to fracture toughness, the strength and hardness of the material is reported, to convey a more complete picture.

Nickel–silicon alloys of the same composition as the alloys described in this paper have good corrosion resistance, particularly in hot sulphuric acid [7]. When fully transformed, they are comprised of Ni_3Si to which the addition of a small amount of boron imparts moderate ductility [8]. Thus, both boron-doped and boron-free materials were examined.

2. Experimental procedure

The alloys were the same materials as used in two earlier studies [9, 10]. They contained Ni–23 at% Si (with and without 0.19 at% boron) and had been extruded from powders into rods (26 mm diameter). From the as-received rods, specimens were machined for compression tests and three-point notched bend tests. Table I gives their shape and dimensions. After machining, the specimens were annealed in dried and de-oxygenated argon at 1100 °C for a period from 5 min to 48 h to obtain different Ni(Si) particle sizes within the matrix, and then air cooled. (While quenching following the high-temperature anneal would have been desirable to suppress the peritectoid phase transformation (see below), such rapid cooling cracked the material). Subsequently, the specimens were annealed at 300 °C in dried and de-oxygenated argon for 1 h to reduce any internal stresses. Then the bend specimens were notched at the centre of the bottom surface ($S \times B$) using either a diamond saw or the single-edge-precracked-beam method given by Nose and Fujii [11]. The notches were 5.8 mm deep (for both methods) and of root radii 0.11 mm (diamond saw) or about 0.0005 mm (single-edge-precracked-beam). The radii were measured from optical photographs of the notch roots at $\times 200$ magnification. The microstructure of representative specimens was analysed using quantitative metallography [12]. Marble's reagent was employed to reveal the phase boundaries.

All experiments were carried out at room temperature. Both compression and three-point bend tests were performed using a floor-model MTS machine. A clip displacement gauge was mounted on

0022–2461

TABLE I The shape and dimensions of the test specimens

Test	Specimen	
	Shape	Dimension (mm)
Compression	Cylinder	5.1 diameter × 12.7
bend	Rectangular bar	$S = 45.7$, $W = 11.4$, $B = 5.8$

the compression specimens to measure the strains and was mounted across the notches of bend specimens to measure the crack opening displacement (COD). Lubrication powder (MoS_2) was employed between the platens and the compression specimen. The compression tests were performed at a strain rate of $10^{-4}\,s^{-1}$ and the bend tests, at a loading rate of around 1.0 MPa $m^{1/2}\,s^{-1}$.

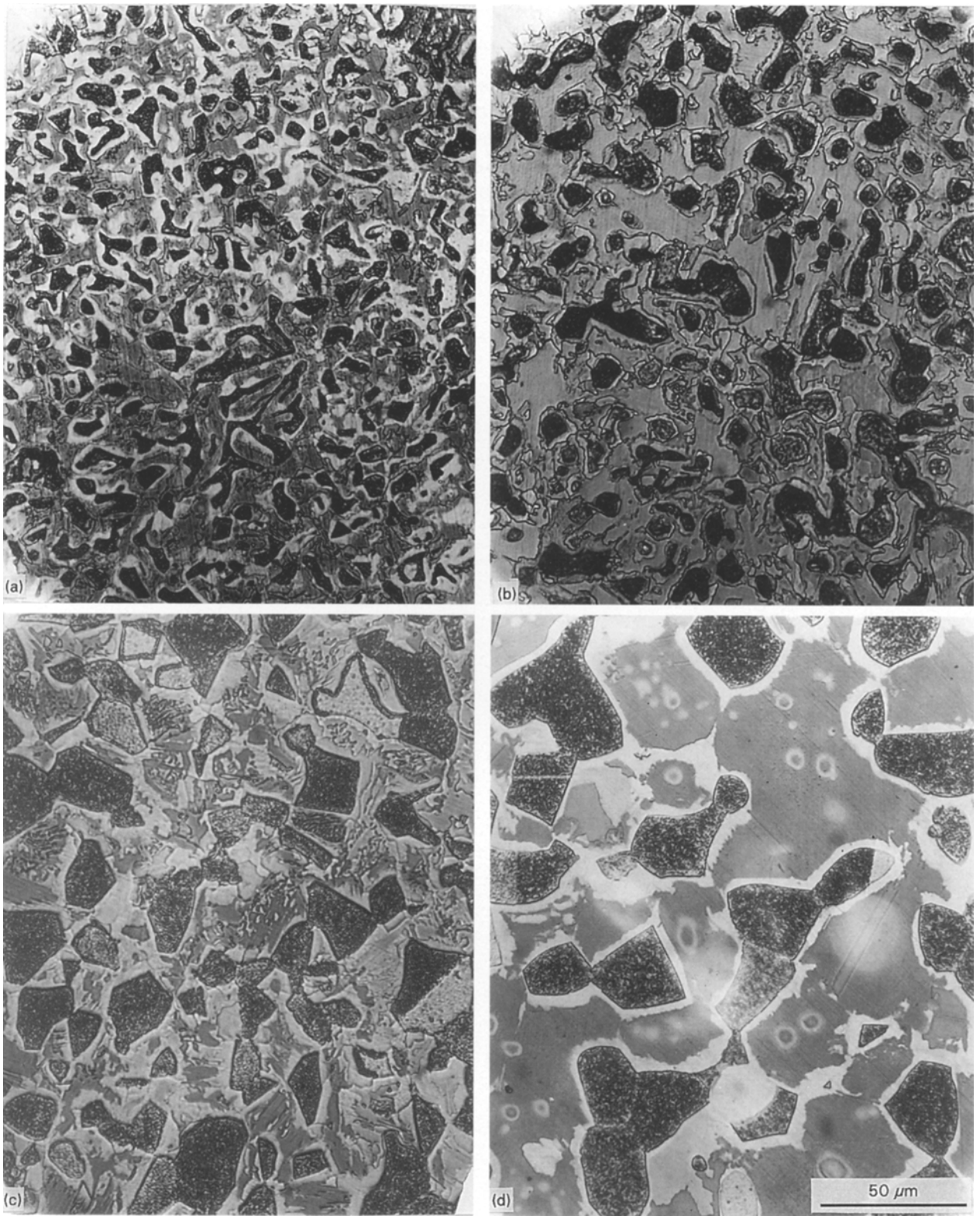

Figure 1 Optical micrographs of (a, c) boron-free and (b, d) boron-doped Ni–23Si alloys after annealing at 1100 °C for (a, b) 0.75 h, (c) 28 h, (d) 48 h followed by air cooling, etched with Marbles reagent.

TABLE II Microstructural parameters of four selected specimens

	Ni–Si–1100 °C–0.75 h	Ni–Si–1100 °C–28 h	Ni–Si + B–1100 °C–0.75 h	Ni–Si + B–1100 °C–48 h
$(V_f)_{Ni(Si)}$	0.22	0.33	0.25	0.28
$(V_f)_{Ni_3Si\ rim}$	0.31	0.22	0.23	0.1
$\lambda_{Ni(Si)}$ (μm)	8.5	20.2	12.0	21.2
$\lambda_{Ni_3Si\ rim}$ (μm)	5.2	13.5	9.1	15.4
$L_{Ni(Si)}$ (μm)	1.6	8.2	2.4	21.2
$L_{Ni_3Si\ rim}$ (μm)	1.7	3.4	1.5	2.9
$S_{Ni(Si)}/V_{Ni(Si)}$ (mm^{-1})	2472	487	1643	189

3. Results and discussion

3.1. Microstructure

Fig. 1 shows optical micrographs of the representative microstructure of specimens with and without boron which had been annealed at 1100 °C for 0.75, 28 and 48 h. In keeping with the Ni–Si phase diagram [13] and TEM analysis [10], the microstructure consisted of Ni(Si) particles (dark phase), Ni_3Si rims (light phase) around the NI(Si) particles, a complex silicide matrix (grey), and Ni_3Si precipitates within the Ni(Si) particles. The precipitates could not be resolved optically, but were seen in transmission electron micrographs [10]; they account for the mottled appearance of the etched Ni(Si) particles, and formed upon cooling after the high-temperature anneal. The rims on the particles formed via a peritectoid transformation during cooling [10].

The matrix was different for the two alloys. Judging from the phase diagram [13] and from earlier TEM analysis on this alloy [10], the matrix for the boron-free alloy was a mixture of Ni_3Si (β_1) of $L1_2$ crystal structure and a complex silicide $Ni_{31}Si_{12}(\gamma)$ [13] of either a hexagonal or a triclinic structure. (Prior to the work by Oya and Suzuki [13], $Ni_{31}Si_{12}$ was written as Ni_5Si_2 and was considered to have a triclinic crystal structure.) This microstructure is formed via the eutectoid decomposition of the high-temperature distorted-Ni_3Si phase (β_2) upon cooling following the coarsening anneal. Its two-phase character, although poorly evident from Fig. 1a and c, is better seen in Fig. 5a below. For the boron-doped alloy the matrix was untransformed β_2, in keeping with the fact that boron, as shown earlier [10], retards the eutectoid transformation.

Table II lists the volume fractions, V_f, interface to interface distances, λ, apparent diameters, $L_{Ni(Si)}$, of the Ni(Si) particles, the thickness, L_{Ni_3Si}, of the Ni_3Si rims (where λ and L are defined in Fig. 2) and the surface area to volume ratio, S/V, of the particles. The parameters were determined from at least six different photographic areas. With increasing time, the Ni(Si) phase coarsened from small, micrometre-sized particles to larger particles. Correspondingly, the volume fraction of the peritectoidally formed Ni_3Si rim decreased, owing to the smaller S/V, even if the rim thickness increased by a factor of 2 with increasing annealing time. Boron appears to have increased slightly the Ni(Si) coarsening rate, as noted earlier [10], but to have decreased the final volume fraction of this phase. The volume fraction of Ni(Si) is lower than the equilibrium fraction (at 1100 °C) calculated from the lever rule, owing to the reaction of Ni(Si) with β_2 during the cooling to produce the Ni_3Si rim.

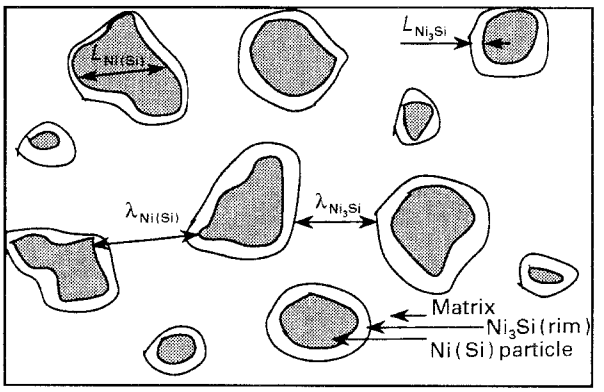

Figure 2 Schematic sketch defining the microstructural parameters of Table II.

In essence, the microstructure consisted of ductile particles (as shown below) dispersed within a brittle matrix. It was complicated by a dispersion of precipitates within the particles and by a rim of Ni_3Si around the particles.

4. Mechanical properties

4.1. Microhardness

The microhardness of the matrix, Ni_3Si rim and Ni(Si) particles was measured using a diamond indentor and 25 g load for 35 s. The surface of the specimens had been polished and etched. Each phase in the microstructure was indented twenty times. No cracking was found even in the brittle matrix, reminiscent of the absence of cracking of the brittle $L1_2$ intermetallic $Al_{67}Ni_8Ti_{25}$ under small loads [14]. The results are given in Table III. In both alloys the particle and the rim are softer than the matrix, although the rim/matrix difference is statistically less significant. Boron appears to increase the hardness of both the matrix and the rim, but not of the particles. The different hardness values of the boron-doped matrix (β_2) and boron-free matrix ($\beta_1 + \gamma$) probably reflect their different microstructures.

4.2. Compressive strength and ductility

Fig. 3 shows typical compressive stress–strain curves. All alloys failed in a brittle manner, although the fracture was delayed (Fig. 3a) within the alloys having the finest microstructure. Microcracks (see below)

TABLE III Microhardnesses of Ni(Si), Ni_3Si, and matrix

Alloy and heat treatment	Microhardness ($kg\ mm^{-2}$)		
	Matrix	Ni_3Si rim	Ni(Si) particle
Ni–23 at % Si–1100 °C–28 h	571–417	451–307	279–219
	494 ± 77	379 ± 72	249 ± 30
Ni–23 at % Si + B–1100 °C–48 h	683–503	537–361	259–223
	593 ± 90	449 ± 88	241 ± 18

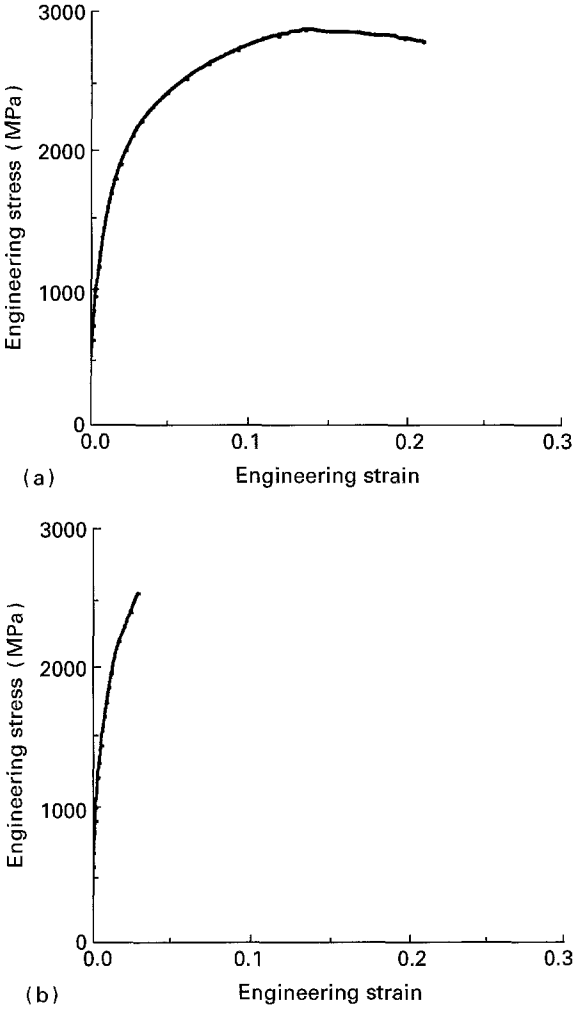

Figure 3 Typical engineering stress versus strain for Ni–Si after annealing at 1100 °C for (a) 0.75 h and (b) 28 h, deformed under uniaxial compression at room temperature at $10^{-4}\ s^{-1}$.

formed within the matrix during the deformation, causing the material to fracture either into many small pieces (in σ–ε curves like Fig. 3a) or into two pieces through axial splitting (for σ–ε curves like Fig. 3b). It appears that at least some of the inelastic strain was caused by the internal microcracking.

Fig. 4 plots the yield (at 0.2% offset) and the fracture strength versus the annealing time. To a first approximation, little effect is apparent of both the annealing time (i.e. particle size) and the boron (i.e. single-phase β_2 matrix versus two-phase $\beta_1 + \gamma$ matrix).

With the exception of the alloys annealed for the shortest time (75 min), the failure strain showed no systematic dependence upon annealing time. For both

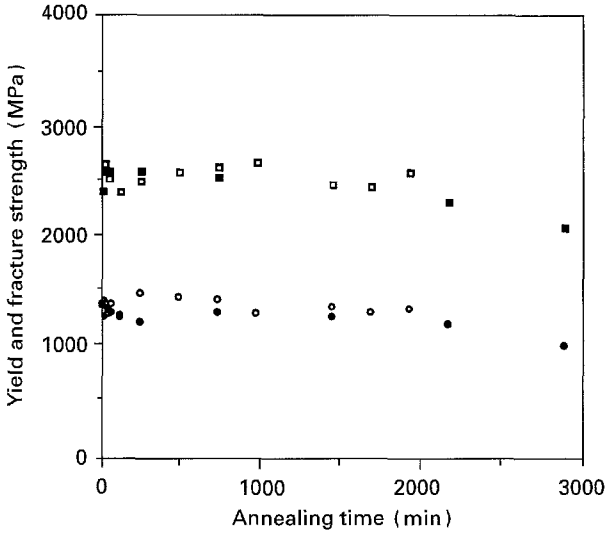

Figure 4 (○, ●) Yield and (□, ■) fracture strength versus annealing time at 1100 °C for (○, □) Ni–Si and (●, ■) Ni–Si + B. Yield stress taken at 0.2% strain.

alloys, the ductility ranged between 2 and 10% with most of the data falling near the lower limit. Because the compressive failure depends upon the propagation of microcracks, the scatter in the ductility may reflect the distribution of cracks, those nearer the free surface propagating more easily than those nearer the centre of the specimen.

A boron-free sample compressed 2.3% was cut transversely, polished, etched, and examined by SEM, Fig 5a. Also, the longitudinal free surface of a boron-doped sample, was polished and etched before compressing 6.9% and then examined by SEM, Fig. 5b. (Note the two matrix phases within the boron-free alloy, Fig. 5a; these illustrate the eutectoid decomposition, noted above.) Fig. 5a shows that after only 2.3% compression microcracks formed within the γ-phase of the matrix and stopped at the Ni_3Si rim. Fig. 5b shows that after greater compression, one matrix microcrack (A) penetrated the Ni_3Si rims and then stopped within the Ni(Si) particles; another crack (B) passed along the β_2/Ni_3Si rim boundary. Correspondingly, the fracture surface, Fig. 6, showed dimpled regions (A) immersed within a field of cleavage. From their morphology and size, the dimpled regions correspond to Ni(Si) particles which fractured in a ductile mode. Fig. 6 also suggests that the Ni_3Si rim (B) fractured via cleavage. These observations show that the Ni(Si) particles absorb energy through plastic deformation, which probably accounts for the relatively large ductility of the alloys.

That the Ni(Si) particles are effective barriers to crack propagation was also seen in an indentation experiment using a spherical (i.e. macrohardness) indentor. Examination of the region adjacent to the indentation, Fig. 7, showed that a crack which propagated part-way through the matrix was stopped by the particles (A and C) and by the rim (B).

4.3. Fracture toughness

Table IV gives the fracture toughness, or K_Q, for both alloys for each heat treatment. The load versus COD curves from the bending tests (for both sharp and blunt notches) were essentially straight lines, and so the calculation of K_Q followed the standard procedure described in ASTM specification E-399. The K_Q measured is actually K_{Ic}, because the three-point bending specimens were thick enough to satisfy the condition: $B,\ a > 2.5\ (K_Q/\sigma_y)^2$. For instance, K_Q of one of the specimens of Ni–Si–1100 °C–0.75 h was 19.7 MPa $m^{1/2}$, and the yield strength was 1290 MPa, giving 2.5 $(K_Q/\sigma_y)^2 = 0.6$ mm; this value is much smaller than both the thickness and the crack length of 5.8 mm. Every result was analysed through this procedure. The root radius of the crack tip (0.11 mm or about 0.0005 mm) had little, if any, effect. Also, the annealing time and the addition of boron had no systematic effect, although the fracture toughness values of the alloys annealed for 45 min appeared to

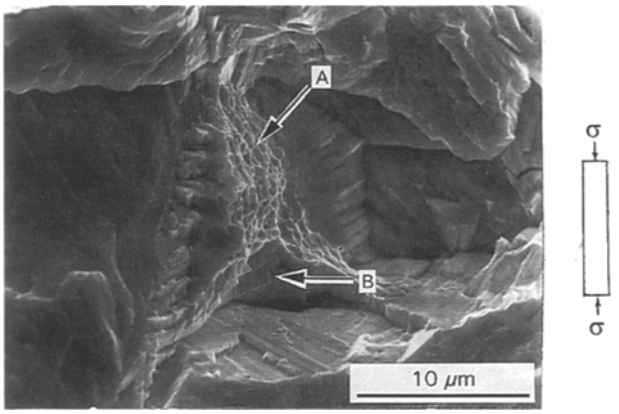

Figure 6 Plastic stretching + microvoid coalescence fracture mode of Ni(Si) phase (A), crystallographic fracture of the Ni_3Si rim (B), and cleavage fracture of the β_2 matrix exhibited in the Ni–Si + B–1100 °C–36 h.

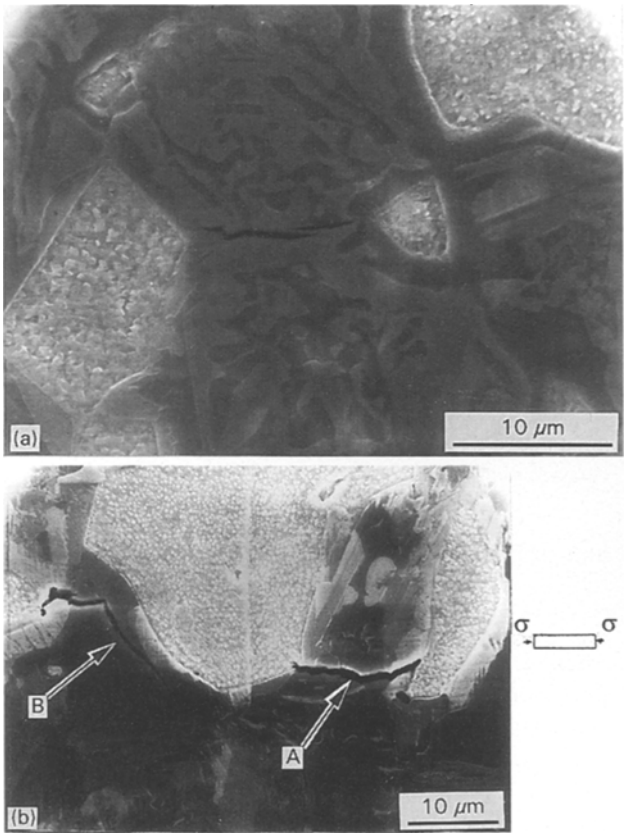

Figure 5 Microcracks within the matrix after a few per cent compression. (a) Ni–Si–1100 °C–28 h (e = 2.3%) transverse section. (b) Ni–Si + B–1100 °C–20 h (6.9%) free surface.

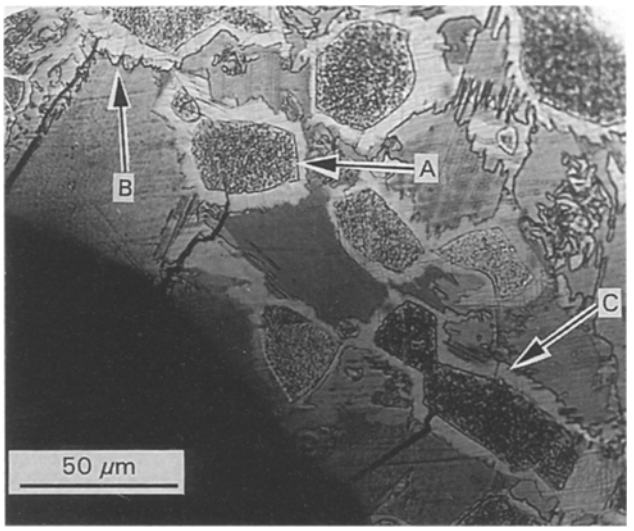

Figure 7 Interaction of Ni(Si) particles (A and C) and Ni_3Si rim (B) with microcracks adjacent to an indentation. Ni–Si + B–1100 °C–48 h.

TABLE IV Fracture toughness, K_Q, as a function of alloy and heat treatment

Alloy	Heat treatment	K_Q (MPa $m^{1/2}$) at room temperature	
		Diamond saw notch[a]	Pre-cracked notch[b]
Ni–23 at % Si	1100 °C–0.75 h–air cool, then 300 °C–1 h	19.7, 22.6	
	1100 °C–28 h–air cool, then 300 °C–1 h	16.3, 13.2	15.2
Ni–23 at % Si + B	1100 °C–0.75 h–air cool, then 300 °C–1 h	18.4, 17.7, 22.0	18.6, 17.1
	1100 °C–48 h–aircool, then 300 °C–1 h	13.0	16.4

[a] Specimens were notched by a diamond saw with root radius of 110 μm.
[b] Specimens were precracked by a single-edge-precracked-beam method with root radius of about 0.5 μm [11].

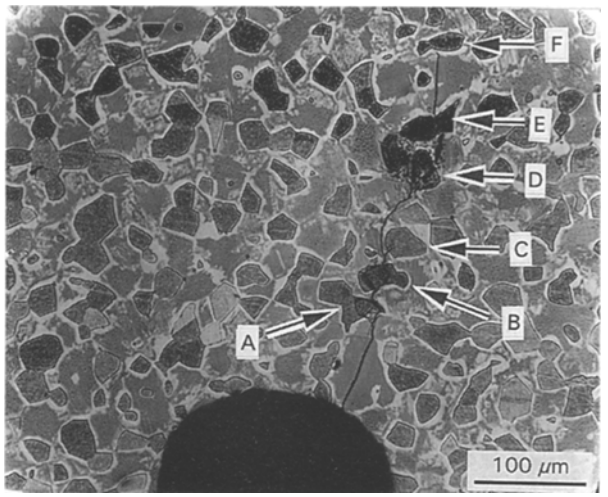

Figure 8 Optical micrograph showing the crack path at the tip of a notch observed in Ni–Si + B–1100 °C–48 h. The crack entered the matrix from the root of the notch, passed through a rim and through particle A, and back into the matrix; it appears to be bridged by particles B, D and E; along its path, one branch stopped within particle C while the main branch went along the matrix/rim interface (at C).

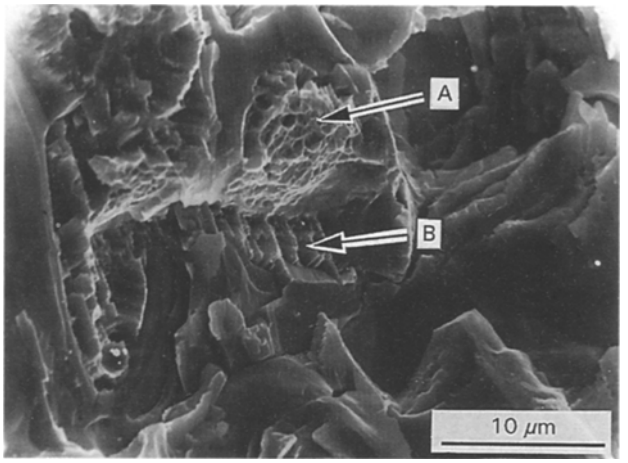

Figure 9 Scanning electron micrograph showing the fracture mode of the Ni(Si) particles (A), the rim on the particles (B) and the matrix observed in bending sample. Ni–Si–1100 °C–28 h.

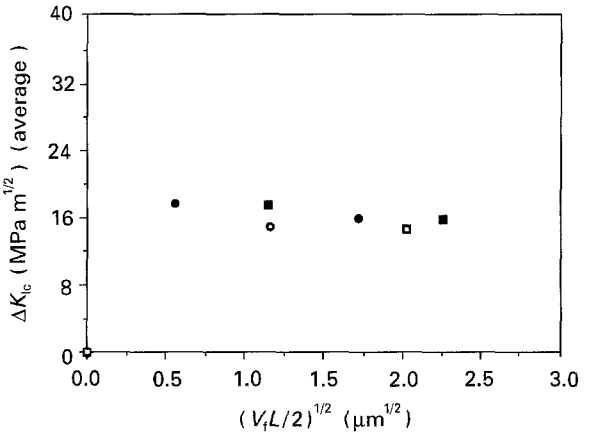

Figure 10 Fracture toughness increment as a function of $(V_f L/2)^{1/2}$. (○, □) Boron-free and (●, ■) boron-doped alloys. Points were obtained using (○, ●), $L = L_{Ni(Si)}$ and (□, ■) $L = L_{Ni(Si)} + L_{Ni_3Si}$.

be slightly greater, owing perhaps to the finer microstructure. It appears, therefore, that the fracture toughness of the material is 17.5 ± 3.0 MPa m$^{1/2}$.

The fracture toughness is relatively high for a silicide intermetallic. For Nb_5Si_3, for instance, K_{Ic} is smaller; i.e. around 1–2 MPa m$^{1/2}$ [5]. Presumably, the fracture toughness of the particle-free matrix of either $\gamma + \beta_1$ or β_2, is also small, given the propensity for cleavage of the β_2 phase.

Optical microscopy showed that when cracks propagated during bending, they took four paths: through the matrix; through the matrix and along the matrix/rim interface; through the matrix, through the rim then along the rim/particle interface; and as the previous path, but through the particle instead of along the particle/rim boundary. Fig. 8 illustrates these paths. Although a step-by-step sequence was not observed, the particles, it is imagined, first bridged the cracks and then fractured in a ductile mode. The last point was evident from SEM fractography, Fig. 9, where again on every specimen ductile regions (A) were seen within a cleaved matrix. The size of the ductile zones is similar to the size of the Ni(Si) particles, implying again that these regions are fractured particles. The SEM fractography revealed crystallographic fracture zones (B) between the particles and the matrix, Fig. 9, again suggesting that the Ni_3Si rim fractured on certain crystallographic planes. It would appear, therefore, that the relatively high toughness of the present alloys originates primarily in the plastic deformation and the ductile fracture of the Ni(Si) particles.

Why the variations in the microstructure had little systematic effect on the fracture toughness is curious. Two theories [15, 16], for instance, suggest that the fracture toughness increment, (ΔK_c), is proportional to the square root of the product of the particle strength, σ_o, the volume fraction, V_f, of the particles and size, L, of the particles; i.e.

$$\Delta K_c \propto (\sigma_o V_f L)^{1/2} \quad (1)$$

where L is either the apparent diameter of the Ni(Si) phase or the diameter of the combined particle plus rim. Assuming that the fracture toughness of the matrix is very small, then the value measured is essentially the same as the increment. Fig. 10 plots the fracture toughness of the alloy versus $(V_f L)^{1/2}$ using both measures of L. No effect is apparent. The origin of the discrepancy between theory and experiment is not clear. Possibly, it can be explained in terms of an attendant reduction in the strength of the composite particles, for as the product $(V_f L)^{1/2}$ increased, the volume fraction of the harder Ni_3Si rim decreased (the hardness of the rim with and without boron is greater than that of the Ni(Si) core, as indicated above). Correspondingly, σ_o should have decreased, because hardness and strength are related [17].

4. Conclusions

From measurements at room temperature of the mechanical properties of a complex nickel silicide, the

following conclusions are drawn.

1. The incorporation of ductile particles of Ni(Si) imparts significant compressive ductility and fracture toughness to an otherwise brittle intermetallic.

2. The ductility and the toughness are attributed to the plastic deformation and ductile fracture of the crack-stopping Ni(Si) particles.

3. Over the size range from $\simeq 1.6$–21 μm and the volume fraction range from $\simeq 0.2$ to $\simeq 0.3$, neither the strength nor the fracture toughness depend upon the distribution of the Ni(Si) particles.

Acknowledgements

The authors thank Gary A. Kuehn and Doug Jones for help and for the use of the Thayer School Ice Lab MTS facility. The use of the Dartmouth College Electron Microscope facility is gratefully acknowledged. This work was supported by the US Department of Energy, Office of Basic Energy Science, grant number DE-FG02-86ER 45260.

References

1. C. K. ELLIOT, G. R. ODETTE, G. E. LUCAS and J. W. SHECKHERD, in "High Temperature/High Performance Composites", Proceedings of the Materials Reserach Society Symposium, Vol. 120 (1988) p. 95.
2. G. R. ODETTE, B. L. CHAO, J. W. SHECKHERD and G. E. LUCAS, *Acta Metall.* **40**, (1992) 2381.
3. P. R. SUBRAMANIAN, M. G. MENDIRATTA, D. B. MIRACLE and D. M. DIMIDUK, in "Intermetallic Matrix Composites", Proceedings of the Materials Research Society Symposium, Vol. 194 (1990) p. 147.
4. J. D. RIGNEY, J. J. LEWANDOWSKI, L. MATSON, M. G. MENDIRATTA and D. M. DIMIDUK, in "High Temperature Ordered Intermetallic Compounds IV", Proceedings of the Materials Reserach Society Symposium, Vol. 213 (1990) p. 1001.
5. M. G. MENDIRATTA, J. J. LEWANDOWSKI, and D. M. DIMIDUK, *Metall. Trans.* **22A** (1991) 1573.
6. T. TAKASUGI, M. NAGASHIMA and O. IZUMI, *Acta Metall.* **38** (1990) 747.
7. W. C. OLIVER, in "High Temperature Ordered Intermetallic Alloys III", Proceedings of the Materials Research Society, Vol. 133, (1989) 397.
8. A. I. TAUB, C. L. BRIANT, S. C. HUANG, K.-M. CHANG and M. R. JACKSON, *Scripta Metall.* **20** (1986) 129.
9. E. M. SCHULSON, L. J. BRIGGS and I. BAKER, *Acta Metall*, **38** (1990) 207.
10. I. BAKER, J. YUAN and E. M. SCHULSON, *Metall. Trans.* **22A** (1992) 1993.
11. T. NOSE and T. FUJII, *J. Am. Ceram. Soc.* **71** (1988) 328.
12. R. T. DEHOFF and F. N. RHINES (eds), "Quantitative Microscopy", (McGraw–Hill, New York, NY, 1968).
13. Y. OYA and T. SUZUKI, *Z. Metallkde*, **21** (1983).
14. C. D. TURNER, W. O. POWERS and J. A. WERT, *Acta Metall.* **37** (1989) 2635.
15. M. F. ASHBY, F. J. BLUNT and M. BANNISTER, *ibid.* **7** (1989) 1847.
16. K. S. RAVICHANDRAN, *Scripta Metall.* **26** (1992) 1389.
17. D. TABOR, "Hardness of Metals" (Clarenden Press, London, 1951).

Received 8 March
and accepted 14 November 1994